FLOWFIELD MEASUREMENTS OF REVERSE FLOW ON A HIGH ADVANCE RATIO ROTOR

Andrew H. Lind
alind@umd.edu
Assistant Research Engineer

Lauren N. Trollinger
ltrolley@umd.edu
Graduate Research Assistant

Field H. Manar
fmanar@umd.edu
Graduate Research Assistant

Inderjit Chopra
chopra@umd.edu
Distinguished University Professor

Anya R. Jones
arjones@umd.edu
Associate Professor

Department of Aerospace Engineering
University of Maryland, College Park, MD 20742

A 1.7 m-diameter Mach-scaled slowed rotor was tested at advance ratios up to $\mu = 0.9$ and three shaft tilt angles $\alpha_\mathrm{s} = -4^\circ,\ 0^\circ,\ 4^\circ$. Two-component time-resolved particle image velocimetry was used to characterize the flow field around a blade element in the reverse flow region, nominally positioned at $\psi = 270^\circ$ and $y/R = 0.4$. Four dominant flow structures were observed: the reverse flow starting vortex, the blunt trailing edge wake sheet, the reverse flow dynamic stall vortex, and the tip vortex. As advance ratio increases, the duration of reduced time that the blade element spends in the reverse flow region also increases. This affects the strength, trajectory, and predicted vortex-induced pitching moment of the reverse flow dynamic stall vortex. Shaft tilt angle also has a strong effect on the evolution of the reverse flow dynamic stall vortex with forward shaft tilt resulting in dramatically increased strength and size. The results of this characterization and sensitivity study are aimed at informing the development of unsteady reverse flow models for use in comprehensive rotorcraft codes.

1. NOMENCLATURE

A	Area, m^2
c	Chord, m
$c_{\mathrm{l_v}}$	Sectional lift due to vortex
$c_{\mathrm{m_v},\,3c/4}$	Sectional pitching moment due to vortex about aerodynamic three-quarter chord
R	Rotor radius, m
s	Reduced time (semi-chords traveled)
U_P	Inflow component of local velocity, m s^{-1}
U_T	In-plane component of local velocity, m s^{-1}
U_∞	Freestream, m s^{-1}
x	Blade-frame chordwise coordinate, m
X	Lab-frame streamwise coordinate, m
y	Radial station, m
Y	Lab-frame out of plane coordinate, m
z	Blade-frame chord-normal coordinate, m
Z	Lab-frame vertical coordinate, m
α	Angle of attack, deg
α_s	Shaft tilt (positive forward), deg
β	Flap angle, deg
Γ_v	Vortex circulation, m^2 s^{-1}
θ_0	Collective, deg
θ_{1s}	Longitudinal cyclic, deg
θ_{1c}	Lateral cyclic, deg
μ	Advance ratio
ψ	Azimuth, deg
ω	Vorticity about Y-axis, s^{-1}
ω^+	Positive (CCW) vorticity about Y-axis, s^{-1}
Ω	Rotor angular rate, rad s^{-1}
BTEWS	Blunt trailing edge wake sheet
RFR	Reverse flow region
RFSV	Reverse flow starting vortex
RFDSV	Reverse flow dynamic stall vortex
TV	Tip vortex

Presented at the 43rd European Rotorcraft Forum, Milan, Italy, September 12-15, 2017.

2. INTRODUCTION

The objective of the present work is to begin experimentally characterizing the flow environment encountered by the retreating blade of a Mach-scaled rotor operating at high advance ratios. The results presented here were collected alongside hubload measurements to assess the performance and vibrations the rotor with carefully balanced uninstrumented blades[1]. Previous work by the authors has provided

extensive airload, surface pressure, and flowfield data for two-dimensional conventional and double-ended rotor blade sections over $0^\circ \leq \alpha \leq 360^\circ$[2],[3], a detailed description of the separated unsteady flow regimes on static blade sections in reverse flow[4], and an analysis of dynamic stall on a sinusoidally pitching[5] and linearly pitching[6] NACA 0012 in both forward and reverse flow. Reverse flow over conventional blade sections was found to separate at low angles of attack, leading to deep dynamic stall in which the number of shed vortices depends on pitching kinematics[5]. This flow was well predicted by numerical simulations[7].

The reverse flow dynamic stall vortex (RFDSV) is an unsteady flow feature that is believed to be a dominant source of unsteady airloads in the reverse flow region. The RFDSV has been studied experimentally by Hiremath et al. using phase-averaged PIV on a sub-scale rotor operating at advance ratios up to $\mu = 1.0$, but with a relatively low maximum advancing tip Mach number of 0.08[8]. The present work builds on the authors' prior two-dimensional experimental and computational efforts[7] by investigating the reverse flow region of a Mach-scale rotor operating at advance ratios up to $\mu = 0.9$ with a maximum advancing tip Mach number of 0.45. Previous unsteady surface pressure measurements have provided evidence of RFDSV convection on the same sub-scale model rotor used in the present work[9], as well as on a full-scale slowed UH-60A rotor[10].

The present work aims to provide fundamental qualitative and quantitative insight on the flow structures observed in the reverse flow region. The reverse flow region is highly three-dimensional and the present work is limited to two-dimensional flow measurements with the interrogation plane nominally positioned at a single radial station. Spanwise flow velocity and two of the three components of vorticity were not measured; the influence of these flow quantities on the development of the observed flow structures should not be overlooked. Furthermore, the effects of the observed flow structures on blade loads and dynamics are not described the present work since corresponding pitch-link loads, flap and lag angles, sectional pressure, and blade torsion/bending measurements were not collected.

Despite these limitations, the present work provides a strong qualitative understanding of the spatial and temporal evolution of flow structures in the reverse flow region along with some quantitative characteristics (while noting the lack of spanwise velocity and gradient measurements). This work represents an early step towards experimentally characterizing the entire reverse flow region of a high advance ratio rotor. It is also useful for informing initial development of unsteady aerodynamic models of reverse flow for use in comprehensive rotorcraft codes.

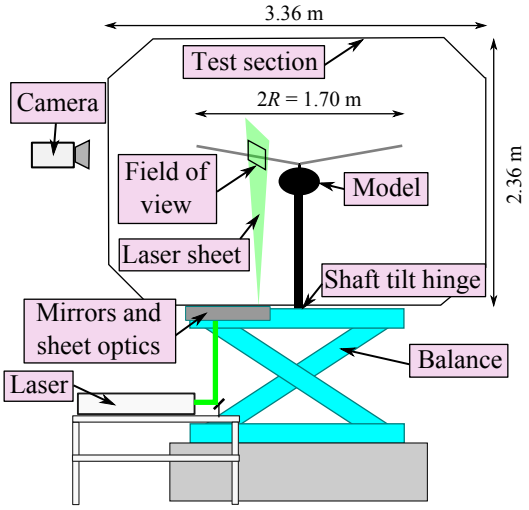

Fig. 1. Sketch of the experimental setup in the Glenn L. Martin Wind Tunnel.

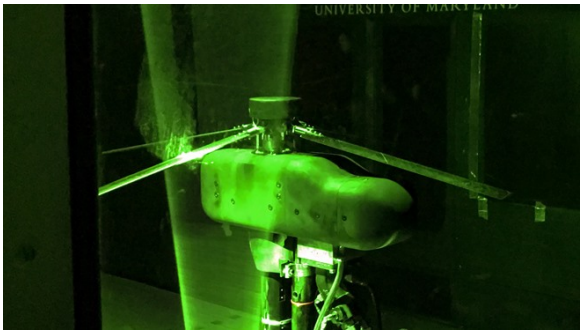

Fig. 2. Photo of the experimental rig and laser sheet installed in the wind tunnel test section.

3. METHODOLOGY

Two-component time-resolved particle image velocimetry (PIV) was performed to investigate the flow around the retreating blade of a sub-scale high advance ratio four-bladed rotor with a diameter of 1.7 m (67 in). Figure 1 shows a sketch of the experimental setup installed in the Glenn L. Martin wind tunnel at the University of Maryland. The rotor rig features a fully articulated hub with an unsteady force balance. The Mach-scaled NACA 0012 blades are untwisted, untapered, and were constructed with carbon fiber wrapped over a foam core and aluminum spar. Each had a chord of 8 cm (3.15 in). A 3-D printed representative fuselage was mounted to the test stand. The shaft tilt angle was adjusted using a hinge located at the base of the rotor stand. During testing, the collective pitch was set to a desired value and the lateral and longitudinal cyclic pitch controls were subsequently adjusted until the rotor was trimmed for zero first-harmonic flapping ($\beta_{1c} = \beta_{1s} = 0^\circ$).

A high-speed laser was located beneath the test section floor in the balance room. A series of mirrors and sheet optics were used to illuminate the retreat-

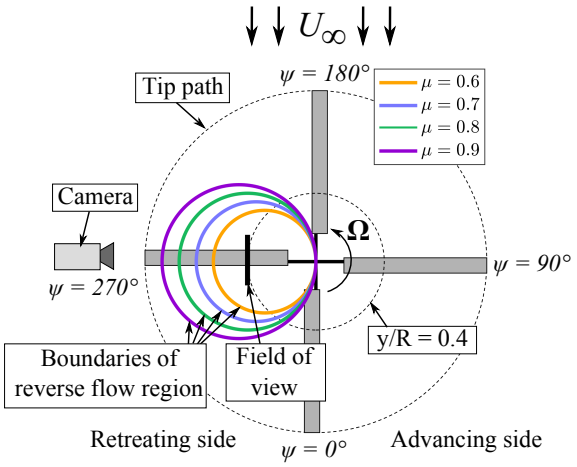

Fig. 3. Scaled drawing of the experimental setup with $\alpha_s = 0°$. The camera position and size is not to scale.

ing blade from below so that the lower surface (i.e., suction side) of the retreating blade could be interrogated. Figure 2 shows the rotor and laser sheet installed in the wind tunnel test section. A 4 MPx high-speed camera was positioned outside the test section and imaged the flow between $700 - 1000$ Hz, depending on the test run. For each test point, between 2700 and 3600 measurements were collected over a time span of approximately 4 s. The camera was aimed radially along $\psi = 270°$. The laser sheet was positioned to illuminated the flow around a blade element positioned at $y/R = 0.4$ when $\psi = 270°$.

Figure 3 shows a scaled drawing of the experimental setup with zero shaft tilt ($\alpha_s = 0°$) to illustrate the relative size of the field of view to the boundary of the reverse flow region. The total field of view measured approximately 3 chords in the streamwise direction and 1.8 chords in the vertical direction. The field of view measured an azimuthal range of approximately $250° \leq \psi \leq 290°$ with $\alpha_s = 0°$. Four advance ratios were considered in the present work. Advance ratio was varied via a change in freestream while the rotor speed was held constant at 15 Hz (900 RPM).

Note that Figure 3 shows that while the field of view for the PIV is inherently straight and aligned with the freestream, the path taken by the $y/R = 0.4$ blade elements is circular. However, the field of view was assumed small enough relative to the curved path of the blade element to sufficiently capture its path. Furthermore, although the flow environment of a rotor is inherently three-dimensional, it is also assumed that the radial flow (and influence of radial flow) is small in the neighborhood of $\psi = 270°$. The validity of the latter assumption will be explored in future work with steroscopic (i.e., three-component) PIV and comparison with CFD simulations.

Multi-pass cross-correlation was performed on the raw PIV measurements with decreasing window size

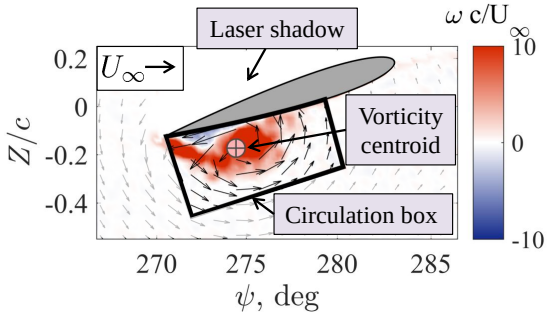

Fig. 4. Illustration of circulation box and centroid calculation using a sample phase-averaged result of the reverse flow dynamic stall vortex (RFDSV).

to 24×24 px and 50 % overlap. The resulting vector resolution was 63 vectors/chord, though for clarity, 1/8 and 1/6 calculated vectors are shown in the X/c- and Z/c-directions for all flowfield results (except Figure which shows 1/4 and 1/3 of the calculated vectors in the X/c- and Z/c-directions).

An image-processing algorithm was written to interpret the raw PIV images and identify the position of the leading edge, trailing edge, or both (when possible). The images in which both the trailing and leading edge were identified were then used to estimate the position of the quarter-chord and blade pitch. The streamwise lab-frame coordinate, X/c, was transformed to azimuth, ψ. A cubic spline fit was applied to the measurements with a "known" quarter-chord azimuthal position in order to interpolate the position of blades for intermediate measurements. This image processing approach was performed due to the fact that the rotary shaft encoder to measure azimuth failed during testing.

Once the blade azimuth for each measurement was identified, phase-averaging was then performed on the processed vector fields with $1°$ azimuthal resolution (approximately $0.07c$) for each of the four individual rotor blades (i.e., to prevent artificial effects from appearing due to dissimilarities in the blade tracks). Typically 8-10 measurements were phase-averaged for each blade at each azimuth. Prior to phase-averaging, the velocity fields were shifted in the streamwise direction so that they coincided with the nominally desired azimuthal angle.

Figure 4 shows a representative phase-averaged result of the reverse flow dynamic stall vortex (RFDSV). The red and blue heatmap of normalized vorticity is overlayed with velocity vectors with the freestream subtracted. An artificial circulation box was used to define a domain over which to characterize the RFDSV. The strength of the vortex, Γ_v was found by integrating the positive vorticity (about the Y-axis) within the circulation box.

$$\Gamma_v = \int \omega^+ \cdot \mathrm{d}A \tag{1}$$

The centroid of positive vorticity within the circulation box was found using Equation 2.

$$x_i = \frac{\int x_i \omega^+ \, \mathrm{d}A}{\Gamma_\mathrm{v}} \text{ for } i = 1,\, 2 \tag{2}$$

Here, $x_1 = x$ and $x_2 = z$. The centroid of vorticity is used in the present work to describe the position of the RFDSV. It should be noted, however, that the centroid of vorticity is calculated based on all vorticity within the circulation box, including the shear layer, and thus may differ slightly from the true local center of rotation. However, its ease of use for near-body calculations (especially when the vortex is small in size) made use of the centroid of vorticity preferable over other vortex identifications methods. Note that for clarity, the circulation box is not shown in flowfield results presented in Section 4.

4. RESULTS

4.1 Overview of Flow Structures

Figure 5 gives an overview of the phase-averaged flow structures typically observed for a representative set of "high collective" rotor conditions ($\theta = 10°$, $\mu = 0.6$, $\alpha_\mathrm{s} = 0°$). Flowfield measurements were acquired at other collective settings, but the present work generally focuses on $\theta_0 = 10°$ since the flow structures are most pronounced at this setting. Figure 5 shows red and blue heatmaps of spanwise vorticity (in the Y-direction) normalized by the chord and freestream. The freestream flow and motion of the blade are from left to right. Velocity vectors are overlaid with the freestream subtracted to more clearly illustrate regions of rotational flow. The blade sketch is positioned based on the results of the image processing technique described in Section 3. The pure white regions located generally above the blade sketch are masked areas representing the laser shadow, reflection, and/or obstruction of the seeding particles by the outboard portion of the blade ($0.4 \leq y/R \leq 1$). The flowfield is shown for five phases with each phase indicating the position of the quarter-chord of the blade. Blade azimuth is shown on the abscissa (transformed from X/c-coordinates) and the lab-frame vertical coordinate is shown on the ordinate with $Z/c = 0$ corresponding to the vertical position of the quarter-chord under static conditions (i.e., wind-off, zero-flap, $\psi = 270°$). The results shown are phase-averages for one of the four blades (i.e., not all four blades) to prevent artificial diffusion of the flow structures due to dissimilarities in the tracks of the blades.

Starting with $\psi = 250°$ (Figure 5, top), the blade begins to enter the field of view, but is preceded by a positive (counter-clockwise) vortex. It is believed that this is a *reverse flow starting vortex* (RFSV) that forms as the blade enters the reverse flow region. The theoretical boundary of the reverse flow region (Figure 3) occurs with zero in-plane velocity $U_T = 0$ (i.e., local freestream). However, the blade element is subject to inflow (U_P) and induced flow due to higher-harmonic flapping (i.e., heaving due to $\beta_{2\mathrm{c}}$, $\beta_{2\mathrm{s}}$, etc.) and pitching. Despite the fact that the blade element is oriented with a negative pitch angle in reverse flow (relative to horizontal, the direction of the freestream), it is believed that the inflow and/or induced flow acts to *increase* the local angle of attack to a positive value. Thus, as the blade element enters the reverse flow region, it behaves like an airfoil starting from rest with a positive angle of attack and the airfoil briefly generates positive lift in the Z/c-direction (i.e., circulation in the CW direction).

Additional discussion on the RFSV will be presented in Section 4.2, however it is worth noting that this vortex is believed to be fairly insignificant since it is formed at the boundary of the reverse flow region where dynamic pressure is low. Furthermore, the RFSV quickly convects away from the blade with the freestream. Thus its influence on the sectional airloads is likely small. However, the RFSV may interact with downstream blades, the fuselage, or any tailrotors (or auxiliary propulsion) and should not be completely ignored.

Returning to $\psi = 260°$ (second row of Figure 5), a cross section of the *blunt trailing edge wake sheet* (BTEWS) is evident, characterized by two layers of opposite-signed vorticity. The BTEWS is even more clearly defined at $\psi = 270°$. It is believed that small-scale vortex shedding occurs within the BTEWS, similar to the *slender body vortex shedding* regime described in prior work[4].

The development of a third flow structure, the *reverse flow dynamic stall vortex* (RFDSV), is illustrated between $260° \leq \psi \leq 280°$. As the blade element progresses through this portion of the reverse flow region, the in-plane velocity component is greatest and likely dominates any inflow or induced flow effects. Consequently, the local flow velocity over the blade section is believed to be closely aligned with with freestream (i.e., horizontal). Flow separates below the sharp aerodynamic leading edge resulting in shear layer that rolls up in to the RFDSV. This behavior mimics the formation of a leading edge vortex that forms over an impulsively started flat plate at an angle of attack. Figure 5 shows that as the blade element progresses through the reverse flow region the size and strength of the vortex increases. During this development of the RFDSV, the centroid of vorticity begins to move aftward slightly, primarily due to the growth of the vortex. This behavior is consistent with observations of an attached leading edge vortex over a flat plate.

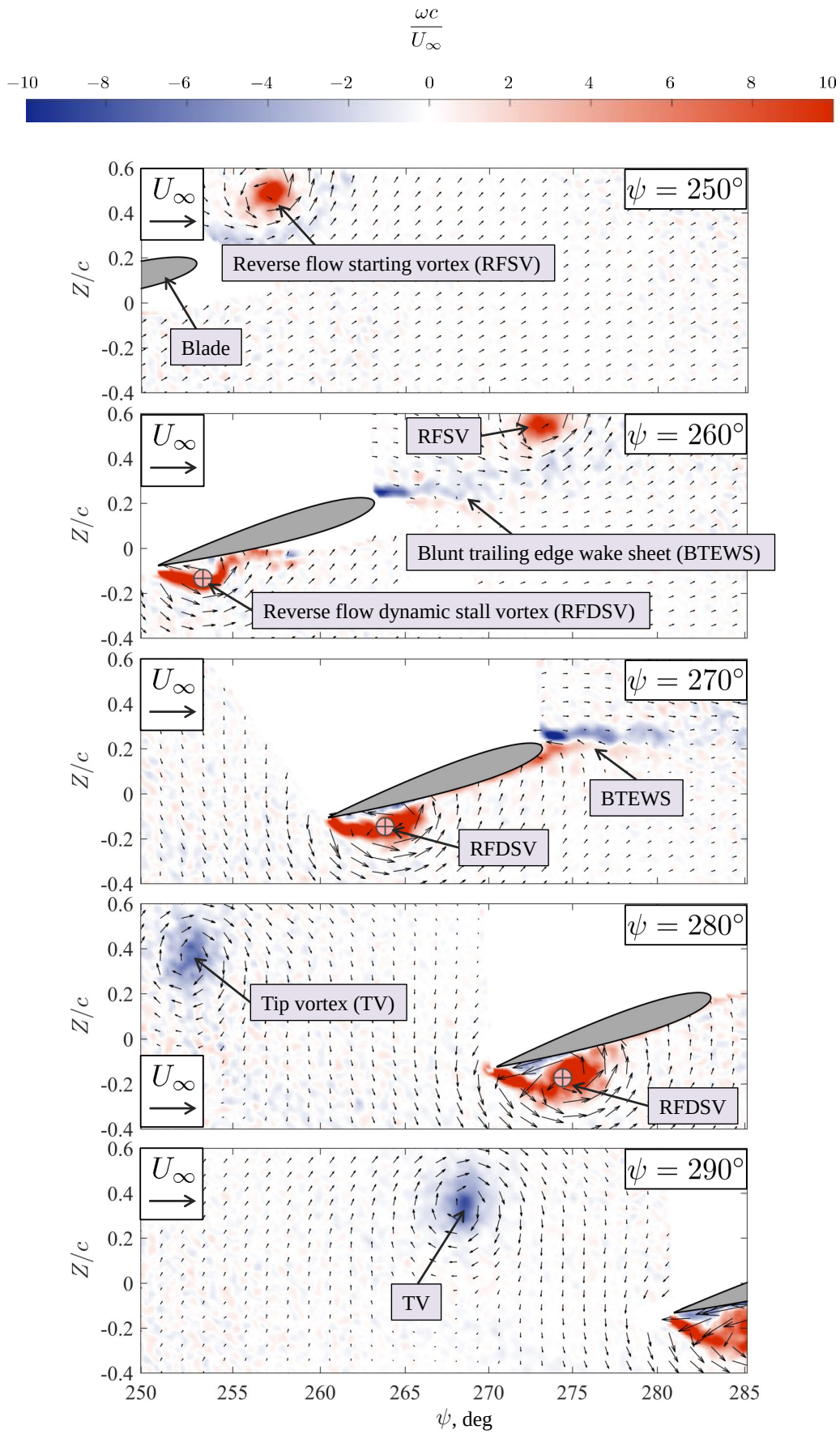

Fig. 5. Variation of phase-averaged vorticity and flow velocity (freestream subtracted) for $250° \leq \psi \leq 290°$ ($0.96 \leq s \leq 3.75$) with $\mu = 0.6$, $\theta_0 = 10°$, and $\alpha_s = 0°$.

Table 1. Rotor conditions for the study of advance ratio effects.

μ	U_∞, m/s	θ_0	θ_{1c}	θ_{1s}	C_T/σ
0.6	48.16	10.0°	−8.9°	4.6°	0.042
0.7	56.08	10.0°	−9.8°	3.7°	0.027
0.8	64.01	10.0°	−9.7°	5.4°	0.014
0.9	72.24	10.0°	−11.0°	4.3°	−0.007

Some of the quantifiable characteristics of the RFDSV such as strength, centroid location, and influence on pitching moment will be detailed in Sections 4.2 and 4.3. However, it is worth introducing here that since the RFDSV grows in size and remains near the aerodynamic quarter-chord (the geometric three-quarter-chord), it is believed that the magnitude of the pitching moment about the geometric quarter-chord (aerodynamic three-quarter-chord) induced by the RFDSV will be high. If the RFDSV persists in the reverse flow region at all blade stations, then the rotor blade is likely to be subjected to a distributed torsion load which could result in high pitch link loads.

The final observed flow structure is a cross section of the tip vortex (TV). The TV is apparent in Figure 5 at the last two selected phases, $\psi = 280°, 290°$. This TV is generated following the swept path of the blade being examined and "catches up" to the blade since it convects with the freestream (which is faster than the blade element in the reverse flow region). The TV is generally located in a plane above the blade, which suggests that either the blade flapped down (relative to the earlier azimuth where the tip vortex was created) or that the inflow velocity is directed upward. This is indirect evidence to support the earlier discussion on the directionality of the reverse flow starting vortex (RFSV).

4.2 Advance Ratio Effects

The advance ratio of the rotor was varied between $0.6 \leq \mu \leq 0.9$ through variation of the freestream while the rotor speed was held constant at 15 Hz. Table 1 shows the pitch controls and flow conditions considered in the present section. Note that collective pitch is constant at $\theta_0 = 10°$ for these cases.

Figure 6 shows phase-averaged flowfields at four advance ratios (rows) and four azimuthal positions (columns). Note that results in the top row ($\mu = 0.6$) are the same as those shown in Figure 5 and are repeated in Figure 6 for direct comparison with flowfields at higher advance ratios. Note that 1/8 and 1/6 of the velocity vectors (freestream subtracted) are shown in the X/c- and Z/c-directions. The acronyms used to label the flow features are consistent with the definitions given in Section 4.1 and in Figure 5.

Beginning with $\psi = 250°$ (left column), the apparent strength of the RFSV decreases with advance ratio. The reason for this is not entirely certain (in part because the initial formation of the RFSV does not occur within the field of view), but it could be due to the fact that as advance ratio increases, the azimuth at which the blade enters the reverse flow region decreases (Figure 3) allowing for more time for the RFSV to diffuse. The cyclic pitch settings also vary with advance ratio (Table 1) thereby changing in the inflow and angle of attack distribution over the rotor disk. This includes the boundary of the reverse flow region where the RFSV is believed to form.

Additionally, the RFSV is positioned further downstream relative to the blade for increasing advance ratio. This is a direct result of the increased freestream velocity relative to the blade velocity. Consider the analytical expression for the in-plane velocity component (i.e., the *local* freestream encountered by a blade element) using dimensional terms.

$$U_T = \Omega y + U_\infty \sin\psi \tag{3}$$

Figure 7(a) shows the variation of in-plane velocity with azimuth for the blade element in the reverse flow region. Note that negative values of U_T are shown since the direction of the flow over the blade element is reversed. The entrance and exit of the blade element from the reverse flow region occurs at $U_T = 0$ which is precisely the same as the intersection of the blade element path and circular reverse flow region boundaries illustrated in Figure 3. Returning to Figure 7(a), it is seen that the in-plane flow velocity (i.e., local freestream) indeed increases with advance ratio. This is consistent with the finding from Figure 6 (left column, $\psi = 250°$) where the RFSV convects further downstream relative to the blade element with increasing advance ratio.

Figure 7(a) illustrates one of the fundamental challenges of characterizing the reverse flow region: the local freestream varies azimuthally and is thus time-variant. For the advance ratios considered here, the local flow velocity begins at zero when the blade element enters the reverse flow region, increases to a maximum at $\psi = 270°$, and then decreases back to zero as the blade element exits the reverse flow region.

Since the blade element experiences a finite journey through the reverse flow region, it is useful to express its history in terms of reduced time, s, which is equal to the number of semi-chords traveled in a flow.

$$s = \frac{2}{c}\int_0^t U(t)\,\mathrm{d}t \tag{4}$$

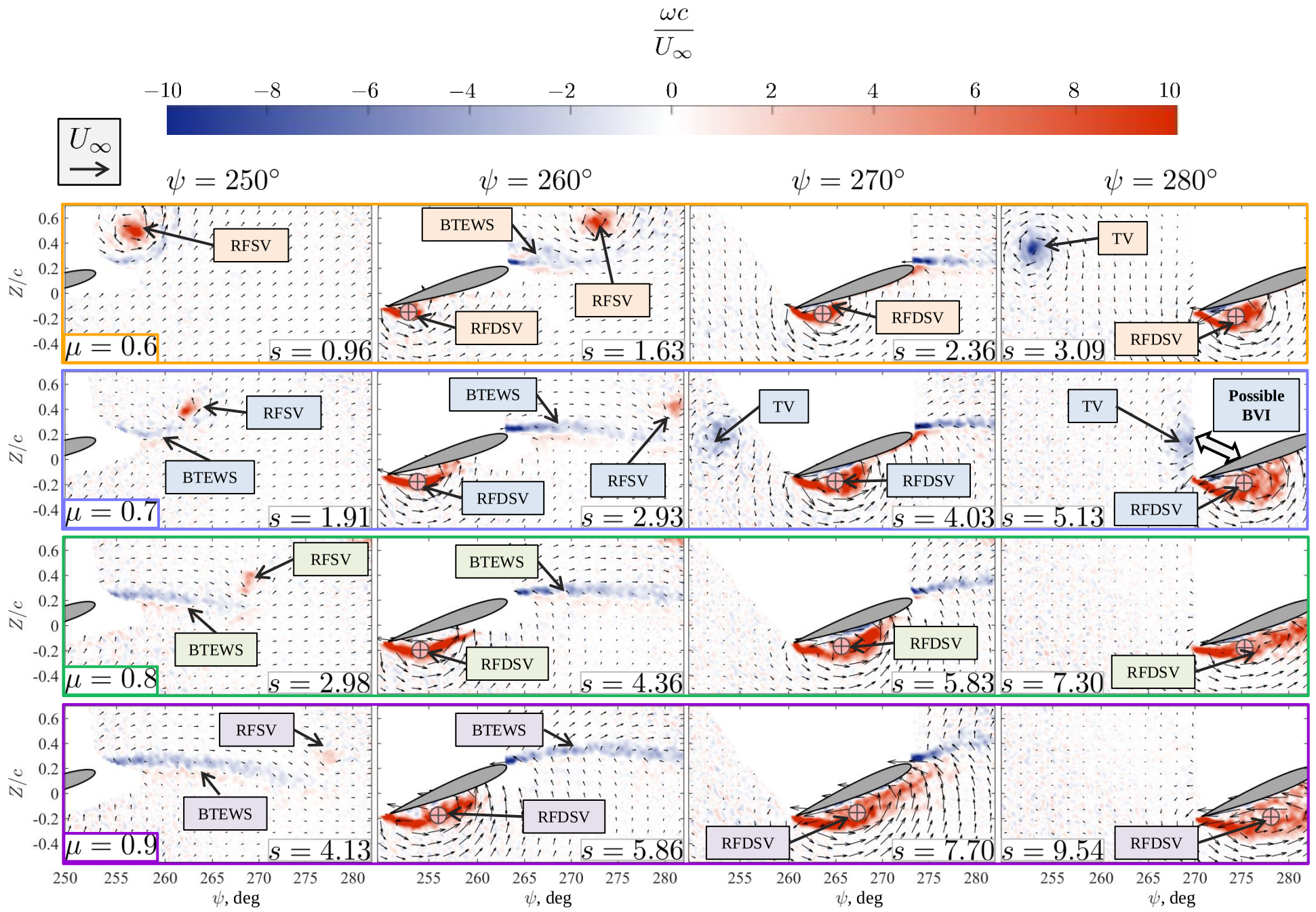

Fig. 6. Effects of advance ration on phase-averaged vorticity and flow velocity (freestream subtracted) for $0.6 \leq \mu \leq 0.9$, $250° \leq \psi \leq 280°$, $\theta_0 = 10°$, and $\alpha_s = 0°$. RFSV: reverse flow starting vortex. BTEWS: blunt trailing edge wake sheet. RFDSV: reverse flow dynamic stall vortex. TV: tip vortex.

Reduced time can also be defined in terms of rotor azimuth and iplane velocity using Equation 5,

$$s = \frac{2}{c} \int_{\psi_{\text{entry}}}^{\psi_{\text{exit}}} \frac{U_T(\psi)}{\Omega} \, \mathrm{d}\psi \tag{5}$$

where ψ is in radians. Figure 7(b) shows the variation of reduced time with azimuth for the blade element at the four advance ratios considered. Four selected phases are indicated with dashed black lines, corresponding to the four columns of flowfields shown in Figure 6. Equation 5 shows that reduced time (Figure 7(b)) is proportional to the integral of the in-plane velocity (Figure 7(a)). Note that in Figure 7(b), $s = 0$ signifies the entry of the blade element into the reverse flow region. The reduced time at the exit from the reverse flow region increases with advance ratio due to the combined effects of the greater in-plane velocities encountered (Figure 7(a)) and the greater size of the reverse flow region (Figure 3). Note that the variation of reduced time is nearly linear in this azimuthal range due to the relatively constant value of $-U_T$ here (Figure 7(a)).

With the relationship between rotor azimuth and reduced time established, attention is turned back to discussing the effects of advance ratio on the flowfield. At $\psi = 260°$ (second column in Figure 6), the reverse flow dynamic stall vortex (RFDSV) is visible below the blade element. The size and strength of the vortex apparently increases with advance ratio. This is a direct consequence of the fact that the reduced time is greater for higher advance ratios at a given azimuth. Figure 7(b) shows that for $\psi = 260°$, the reduced time is $s = 1.63$ for $\mu = 0.6$ whereas it is $s = 5.87$ for $\mu = 0.9$, nearly four times greater. This greater reduced time results in greater vorticity production and subsequent development of the RFDSV. As a result, the centroid of vorticity moves downstream, away from the sharp aerodynamic leading edge. The same relative characteristics of the RFDSV can be seen at $\psi = 270°$ as well; with increasing advance ratio, the vortex is larger, stronger, and positioned further downstream on the chord. A more detailed quantification of the evolution of the RFDSV will be presented after a brief description about the convection of the tip vortex.

In Figure 5 and accompanying discussion, it was shown that the tip vortex "catches up" to the blade that created it since the freestream (which convects the tip vortex) exceeds the speed of the blade element. At $\mu = 0.7$ (second row of Figure 6), the tip vortex is convected even closer to the blade element due the increased freestream relative to the motion of the blade element. Additionally, the tip vortex appears to be weaker (perhaps due to the decreased rotor thrust produced), but travels in the same path as the blade element (perhaps due to the different rotor pitch controls). As a result, the early stages of a

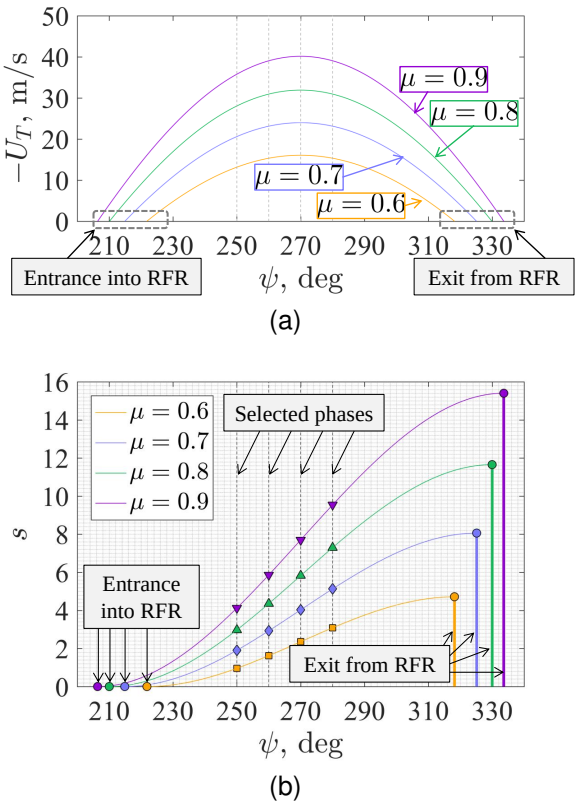

Fig. 7. Theoretical variation of *(a)* in-plane velocity and *(b)* reduced time with azimuth and advance ratio for a blade element at $y/R = 0.4$. RFR: reverse flow region.

possible blade-vortex interaction (BVI) is apparent at $\psi = 280°$. BVIs are well known to be a source of rotor vibrations and noise. Note that the tip vortex is not observed for $\mu = 0.8$ or 0.9. It is believed that the tip vortex is still present, but passes above or below the camera's field of view.

Figures 8 and 9 show quantitative variations of RFDSV characteristics with azimuth (left column) and reduced time (right column). Results are shown for $258° \leq \psi \leq 286°$ in $1°$ increments. The azimuthal domain of Figure 8(c) and all plots in the left column of Figures 8 and 9 is extended to illustrate the entry and exit of the blade element into and out of the reverse flow region. Note that results are not shown for $250° \leq \psi \leq 257°$; the characteristics of the RFDSV could not be identified here since the entire blade element was not in the field of view at these azimuth angles.

Figure 8(a) shows the variation of circulation (in dimensional units) of the RFDSV with azimuth. For a given azimuth, the strength of the RFDSV increases with advance ratio, consistent with the flowfields in Figure 6 and accompanying discussion. Figure 8(b) shows the same values of vortex strength as a function of reduced time. The results appear to generally collapse to a linear trend that is independent of ad-

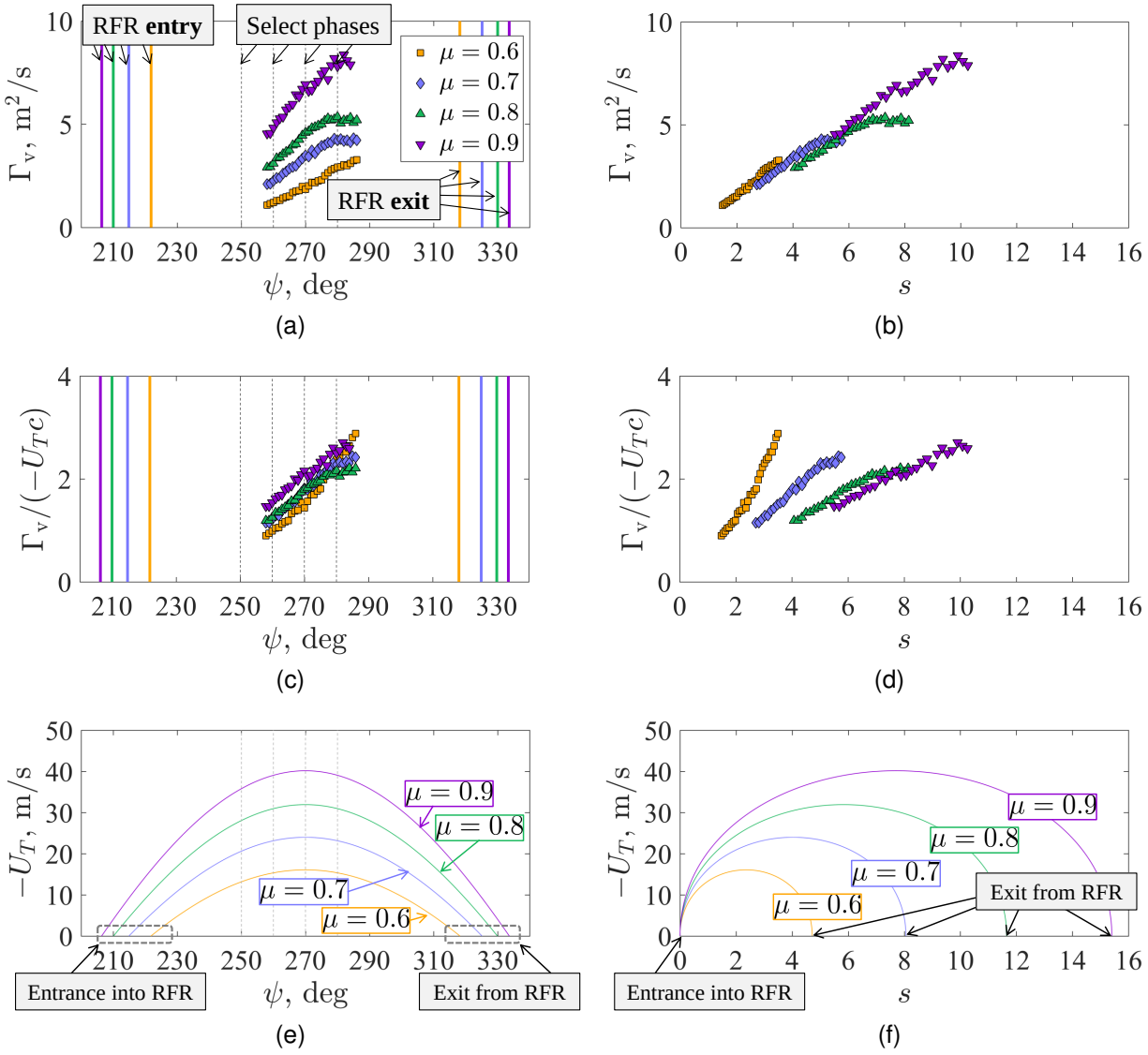

Fig. 8. Effects of advance ratio on the circulation of the reverse flow dynamic stall vortex (RFDSV). *(a, b):* RFDSV strength in dimensional units. *(c, d):* RFDSV strength, normalized by the chord and theoretical local in-plane velocity. *(e, f):* Theoretical in-plane velocity.

vance ratio. If all the spanwise vorticity (i.e., in the Y-direction) is generated at the sharp aerodynamic leading edge where the flow separates, then vorticity production here is generally linearly proportional to reduced time and independent of advance ratio (for the $y/R = 0.4$ blade element between $258° \leq \psi \leq 286°$ and the pitch kinematics given in Table 1).

The use of normalized vortex quantities could be useful for the development of low-order models of the development of the RFDSV. The normalization of vortex strength can be performed using the in-plane velocity component (i.e., the local freestream) and chord. Figures 8(e) and 8(f) show the variation of U_T with azimuth and reduced time. Note that Figure 8(e) is identical to Figure 7(a); it is repeated here to allow for direct comparison with dimensional and normalized vortex strength (Figures 8(a) and 8(c)). Figure 8(c) shows that the normalized vortex strength histories collapse compared to the dimensional vortex strength histories shown in Figure 8(a). Conversely, the variation of normalized vortex strength with reduced time (Figure 8(d)) is fanned out relative to the dimensional vortex strength histories (Figure 8(b)), but they still generally exhibit linear behavior. The range of the magnitude of normalized vortex strength is generally independent of advance ratio due to the increase in in-plane velocity with advance ratio (Figure 8(f)).

Figures 9(a) and 9(b) show the blade-relative chordwise position of the centroid of vorticity. The centroid moves aftward with increasing azimuth and reduced time. This is consistent with the develop-

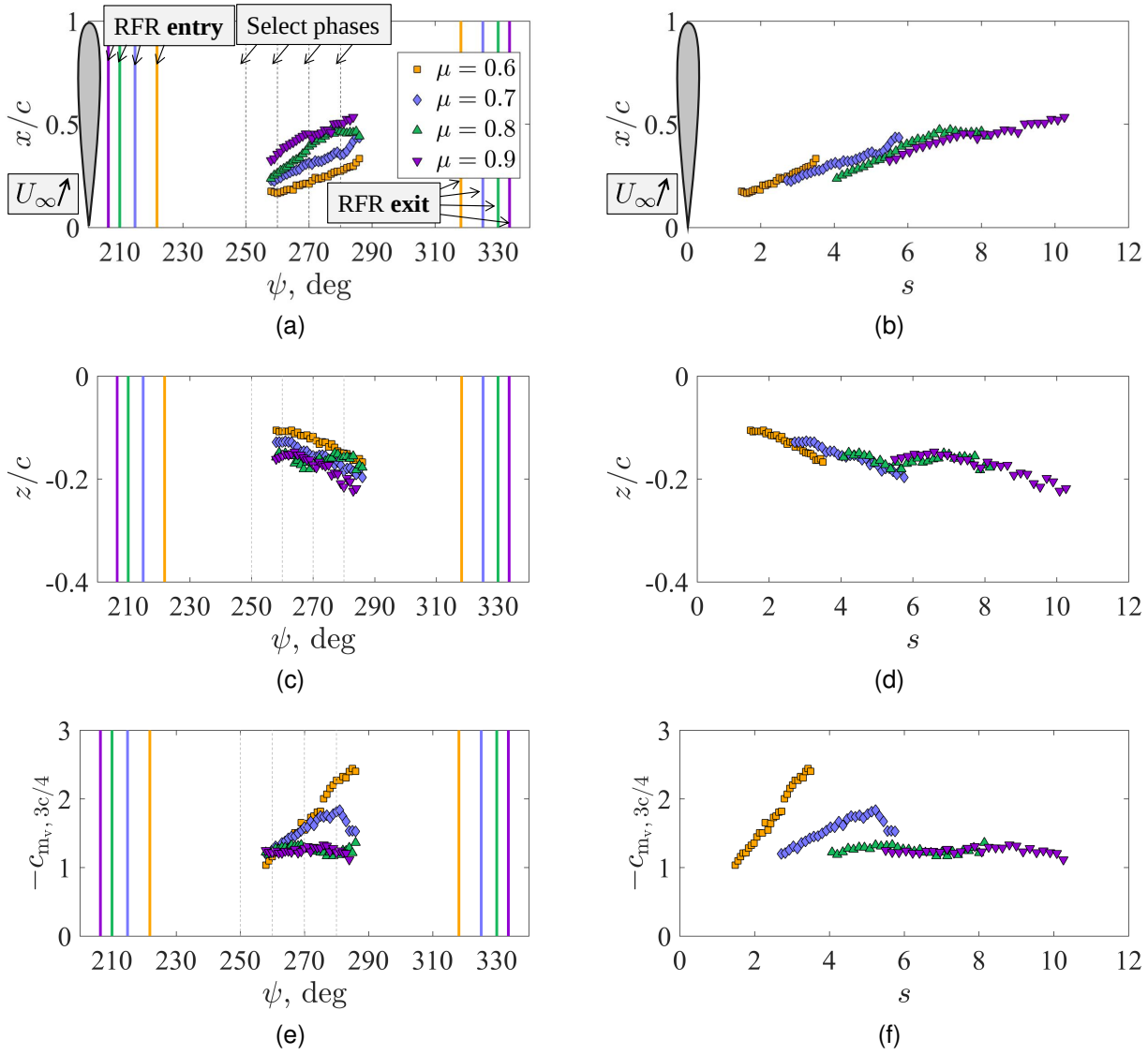

Fig. 9. Additional effects of advance ratio on characteristics of the RFDSV. *(a, b):* Blade-relative chordwise position of vorticity centroid. *(c, d):* Blade-relative chord-normal position of vorticity centroid. *(e, f)* Predicted sectional pitching moment due to the influence of the RFDSV.

ment of the RFDSV in Figure 6 for increasing azimuth. Returning to Figure 9(b), the maximum chordwise location of the centroid is approximately $x/c = 0.5$ for $\mu = 0.9$ after 10 semi-chords of travel. This indicates that the vorticity associated with the RFDSV stays close to the blade element as it passes through the reverse flow region. This is confirmed in Figures 9(c) and 9(d) which show the chord-normal position of the centroid of vorticity. The normal distance away from the chord less than $0.25c$ for all advance ratios considered here. It can then be argued that the RFDSV remains "attached" to the lower surface of the blade element as it passes through the reverse flow region and has a profound effect on the local sectional airloads. This is consistent with prior simulations of a high advance ratio rotor[11].

As was previously mentioned, the fact that the RFDSV generally remains near the aerodynamic leading edge suggests that the pitching moment induced by its presence will be high in magnitude. In the absence of measured sectional pressure distributions, a first-order approximation for the vortex-induced sectional pitching moment using the circulation and centroid position. This simplified approach assumes that the RFDSV decreases the local chordwise pressure distriubution, similar to findings of prior work on a nominally two-dimensional RFDSV[5]. It is further assumed that the net effect of the altered pressure distribution can be represented as a single downward-acting lift vector through the centroid of vorticity (which is an approximation to the vortex center). This assumption is based on prior findings

where the convection of a low pressure front closely matches the convection the center of a RFDSV[5]. It is assumed that the magnitude of this so-called vortex lift is proportional to the circulation of the vortex following the Kutta-Joukowsi theory of lift

$$c_{l_v} = \rho U_T \Gamma_v \tag{6}$$

Using these assumptions, an estimate for the vortex-induced pitching moment about the aerodynamic three-quarter chord (i.e., the geometric quarter chord) can be predicted using

$$c_{m_v,\,3c/4} = -c_{l_v}\left(0.75 - \frac{x}{c}\right) \tag{7}$$

Since Γ_v is positive for the RFDSV, c_{l_v} is also positive. A negative sign has been included on the right hand side of Equation 7 to indicate that c_{l_v} acts downward. Thus, $c_{m,\,3c/4} > 0$ implies a sharp-leading-edge-up pitching moment about the geometric quarter-chord (i.e., counter-clockwise) and $c_{m,\,3c/4} < 0$ implies a sharp-leading-edge-down pitching moment (i.e., clockwise), consistent with convention. Figures 9(e) and 9(f) show the estimated variation of the vortex-induced pitching moment with azimuth and reduced time. Since several assumptions are used to generate this quantity, it is presented here for qualitative purposes only. Note that negative values of $c_{m,\,3c/4}$ are shown on the abscissa (i.e., the magnitude of the sharp-leading-edge-down pitching moment).

At $\mu = 0.6$, the pitching moment increases in magnitude as the blade element passes through the reverse flow region. Since the vortex (i.e., centroid of vorticity) remains near aerodynamic leading edge (Figure 9(b)), the pitching moment behavior is dominated by the rapid increase in the normalized vortex strength (Figure 8(b)). The magnitude of the vortex-induced pitching moment increases from $-c_{m,\,3c/4} \approx 1$ to 2.5 as the blade element passes through the observed portion of the reverse flow region. This could have detrimental effects on local blade torsion and vibrations, though simultaneous measurement of surface pressure, blade torsion, and pitch link loads are needed to confirm this hypothesis. At $\mu = 0.8$ and $\mu = 0.9$, the vortex-induced pitching moment remains nearly constant at $-c_{m,\,3c/4} \approx 1$. This results from a balance between the aft movement of the centroid of the RFDSV toward the aerodynamic three-quarter-chord (Figure 9(b)) and increase in vortex strength (Figure 8(b)).

4.3 Shaft Tilt Angle Effects

Shaft tilt angle was varied between $-4° \leq \alpha_s \leq 4°$ (with $\alpha_s > 0$ implying forward shaft tilt) at a constant advance ratio of $\mu = 0.8$. Table 2 shows the rotor conditions considered in the present section. The case with $\alpha_s = 0°$ is the same as the $\mu = 0.8$ case presented in Section 4.2. Figure 10 shows a sketch of how the tip path plane, blade element path, and boundary of the reverse flow region shifted relative to the field of view during shaft tilt changes. This was due to the fact that the hinge for adjusting shaft tilt angle was located near the test section floor (Figure 1). As a result, the rotor hub physically moved for and aft between test points while the field of view remained fixed. Though this arrangement was not ideal for providing direct comparisons of the flowfield at the same azimuthal locations, insight can still be gained from these results.

Table 2. Rotor conditions for the study of shaft tilt angle effects.

α_s	μ	θ_0	θ_{1c}	θ_{1s}	C_T/σ
$-4.0°$	0.8	$8.0°$	$-9.9°$	$6.5°$	0.042
$0.0°$	0.8	$10.0°$	$-9.7°$	$5.4°$	0.014
$4.0°$	0.8	$10.0°$	$5.2°$	$-2.0°$	-0.024

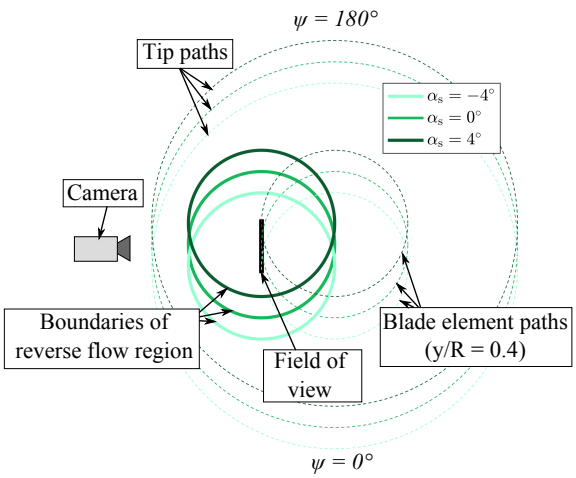

Fig. 10. Sketch of the movement of the reverse flow region relative to the PIV field of view for three shaft tilt angles.

Figure 11 shows flow fields for aft and forward shaft tilt angles. Note that the azimuthal domain is "earlier" in the reverse flow region for $\alpha_s = -4°$ ($244° \leq \psi \leq 265°$ in Figure 11(a)) and "later" in the reverse flow region for $\alpha_s = 4°$ ($268° \leq \psi \leq 290°$ in Figure 11(a)). Following the sequence of azimuths in Figure 11(a), the same progression of flow structures that were observed in the third row of Figure 6 ($\alpha_s = 0°$) are again observed here with some important differences in their characteristics.

Shaft tilt angle has a strong effect on the reverse flow starting vortex (RFSV). Consider the flowfields for $\psi = 240°$ and $250°$ shown in Figure 11(a). The RFSV is is much stronger than the RFSV observed at $\psi = 250°$ with $\alpha_s = 0°$ (Figure 6, first column, third

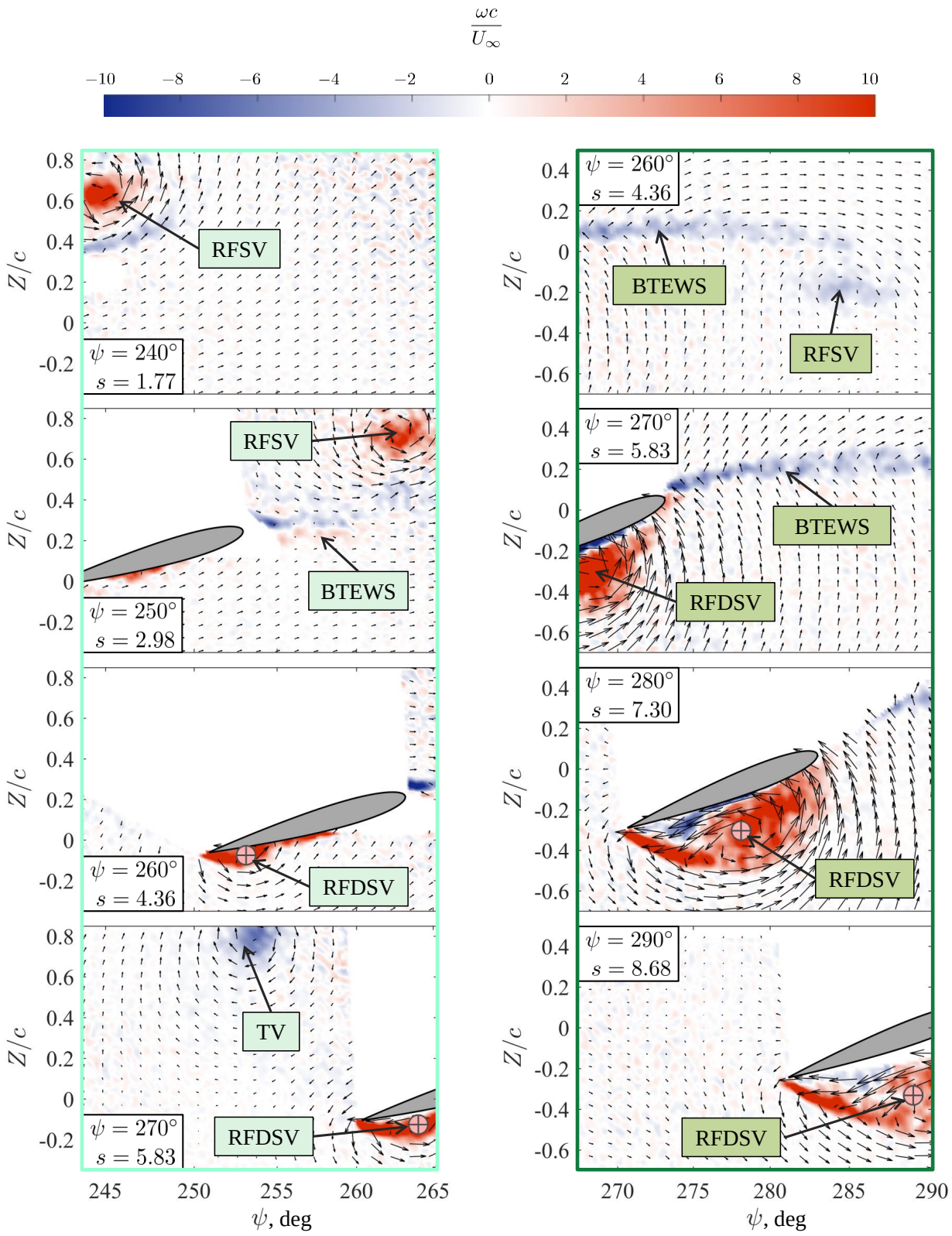

(a) $\alpha_s = -4°$ (aft), $\theta_0 = 8°$.

(b) $\alpha_s = 4°$ (forward), $\theta_0 = 10°$.

Fig. 11. Effects of shaft tilt angle on phase-averaged vorticity and flow velocity (freestream subtracted) for $\mu = 0.8$. RFSV: reverse flow starting vortex. BTEWS: blunt trailing edge wake sheet. RFDSV: reverse flow dynamic stall vortex. TV: tip vortex.

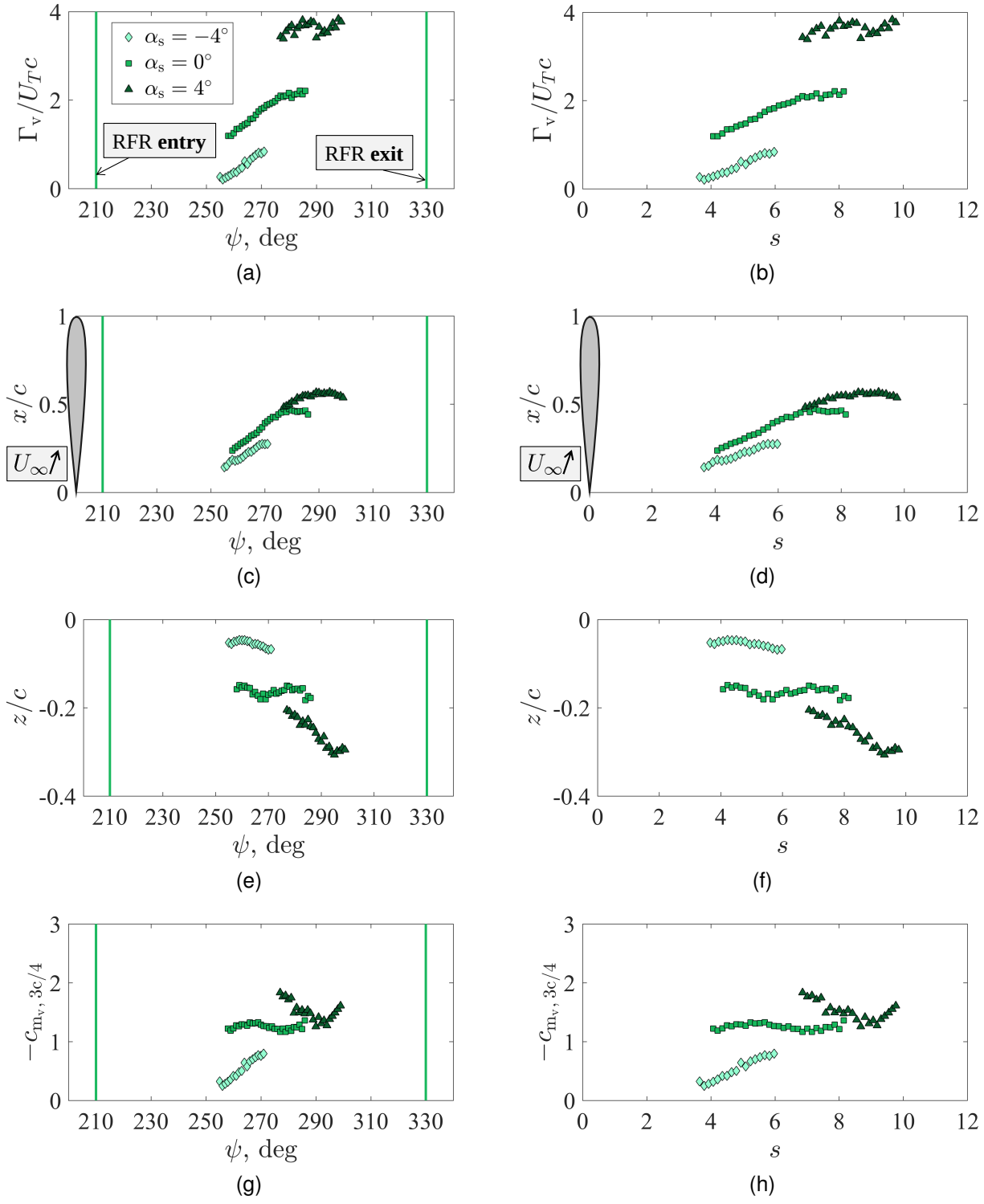

Fig. 12. Effects of shaft tilt angle on characteristics of the reverse flow dynamic stall vortex (RFDSV) at $\mu = 0.8$. *(a, b):* RFDSV strength, normalized by the chord and theoretical local in-plane velocity. RFR: Reverse flow region. *(c, d):* Blade-relative chordwise position of vorticity centroid. *(e, f):* Blade-relative chord-normal position of vorticity centroid. *(g, h)* Predicted sectional pitching moment due to the influence of the RFDSV.

row). Shaft tilt angle acts to alter the inflow distribution; a negative shaft tilt (i.e., aftward) results in an upward-oriented inflow through the rotor disk. This increases the angle of attack encountered by the blade element as it first transitions into the reverse flow region, resulting in a stronger RFSV as observed in Figure 11(a). Conversely, a positive shaft tilt (i.e., forward) results in an increase in downward-oriented inflow through the rotor disk. As the blade element transitions into the reverse flow region, the downward-oriented inflow leads to a negative angle of attack, downward-acting lift, and the formation of a clockwise RFSV (Figure 11(b)).

The development of the RFDSV is also highly sensitive to shaft tilt angle. Figures 12(a) and 12(b) show the variation of normalized vortex strength with azimuth and reduced time at the three shaft tilt angles considered. In general, there is a clear trend that the normalized strength of the RFDSV increases with shaft tilt angle. This is consistent with the previous discussion on the general effect of shaft tilt angle on inflow and angle of attack. A positive shaft tilt angle decreases the angle of attack encountered by the blade element. Since the reverse flow angle of attack is already negative, the magnitude of the negative angle of attack increases with positive shaft tilt. This results in a greater amount of flow separation and a dramatically stronger and larger RFDSV.

The position of the centroid of vorticity is given in Figures 12(c)-12(h). Note that the chord-normal track is much more sensitive to shaft tilt angle than advance ratio (Figures 9(c) and 9(d)) since the RFDSV increases in size with increasing shaft tilt angle. Finally, the vortex-induced pitching moment (Figures 12(g) and 12(h)) is generally higher for positive shaft tilt, but has a nonlinear trend due to the nonlinearity of both the normalized vortex strength (Figures 12(a) and 12(b)) and chordwise position of the vorticity centroid (Figures 12(c) and 12(d)).

5. CONCLUSIONS

The flow environment of the $y/R = 0.4$ blade element in the reverse flow region of a Mach-scale rotor was investigated using time-resolved PIV. The measured flowfields were phase-averaged and highlighted the presence of four flow structures: the reverse flow starting vortex (RFSV), the blunt trailing edge wake sheet (BTEWS), the reverse flow dynamic stall vortex (RFDSV), and the tip vortex (TV). The RFSV, BTEWS, and TV have the potential to interact with downstream bladess. The present work focused on the reverse flow dynamic stall vortex and its sensitivity to advance ratio and shaft tilt angle. Based on these analyses of the RFDSV presented in this work, the following conclusions can be drawn:

1. The total duration (in semi-chords traveled) of the passage of the blade element through the reverse flow region increases with advance ratio. As a result, the RFDSV is generally stronger and positioned further down the chord for a given azimuthal position (e.g., $\psi = 270°$). However, when normalized by local in-plane velocity, the range of vortex strength is generally independent of advance ratio.

2. For the azimuthal range of the retreating blade path observed with $\alpha_s = 0°$ ($250° \leq \psi \leq 290°$), the predicted vortex-induced sectional pitching moment coefficient about the geometric quarter-chord due to the RFDSV varies between $1 \leq |c_{m_v,\, 3c/4}| \leq 2.5$ at $\mu = 0.6$. This large range is due to the fact that the strength of the RFDSV increases with little motion of the centroid of vorticity along the chord, thus resulting in a large moment arm. Conversely, the growth of the RFDSV at $\mu = 0.8$ and $\mu = 0.9$ is balanced with the convection of the centroid of vorticity towards the geometric quarter-chord. As a result, the pitching moment remains nearly constant at $|c_{m_v,\, 3c/4}| = 1$.

3. The shaft tilt angle acts to change the inflow distribution and angle of attack encountered by the blade section in the reverse flow region by altering the inflow distribution. This has a dramatic effect on the evolution of the RFDSV. For $\alpha_s = -4°$, the angle of attack distribution in the reverse flow region is believed to decrease, leading to a weaker RFDSV and relatively low vortex-induced pitching moment ($|c_{m_v,\, 3c/4}| < 1$ for the observed azimuth range). For $\alpha_s = 4°$, the angle of attack distribution in the reverse flow region is believed to increase. The resulting RFDSV is larger and stronger than at other shaft tilt angles due to the effective increase in inflow velocity. This has a moderate influence on the magnitude of vortex-induced pitching moment ($1 \leq |c_{m_v,\, 3c/4}| \leq 2$).

The work presented here provides a fundamental characterization of the flow structures observed for a single blade element in the reverse flow region of a high advance ratio Mach-scale rotor. Future work will be aimed at better understanding the influence of the time-varying and spanwise flow on the evolution of these flow structures over the entire reverse flow region (i.e., at several azimuthal and radial stations). The insight gleaned from the present (and future) work will inform the development of physics-based low-order models for the growth of the reverse flow dynamic stall vortex and its influence on unsteady sectional airloads. Once developed, these unsteady aerodynamic models will be instrumental to accurate prediction of rotor performance and vibrations at high advance ratios.

6. ACKNOWLEDGMENTS

This work was supported by the United States Army/Navy/NASA Vertical Lift Research Center of Excellence Cooperative Agreement with Mahendra Bhagwat serving as Program Manager and Technical Agent, grant number W911W6-17-2-0004. The authors wish to acknowledge Dr. Jewel Barlow, director of the Glenn L. Martin Wind Tunnel (GLMWT), and the GLMWT staff for their invaluable advice and assistance.

7. COPYRIGHT STATEMENT

References

[1]Trollinger, L. N., Wang, X., and Chopra, I., "Refined Measurement and Validation of Performance and Load of a Mach-Scaled Rotor at High Advance Ratios," 43rd European Rotorcraft Forum, 12–15 September 2017.

[2]Lind, A. H., Lefebvre, J. N., and Jones, A. R., "Time-Averaged Aerodynamics of Sharp and Blunt Trailing Edge Static Airfoils in Reverse Flow," *AIAA J.*, Vol. 52, (12), Dec. 2014, pp. 2751–2764.

[3]Lind, A. H. and Jones, A. R., "Unsteady airloads on static airfoils through high angles of attack and in reverse flow," *J. of Fluids and Structures*, Vol. 63, May 2016, pp. 259–279.

[4]Lind, A. H. and Jones, A. R., "Vortex Shedding from Airfoils in Reverse Flow," *AIAA J.*, Vol. 53, (9), Sep. 2015, pp. 2621–2633.

[5]Lind, A. H. and Jones, A. R., "Unsteady Aerodynamics of Reverse Flow Dynamic Stall on an Oscillating Blade Section," *Physics of Fluids*, Vol. 28, (7), Jul. 2016, pp. 1–22.

[6]Smith, L., Lind, A. H., Jacobson, K., Smith, M. J., and Jones, A. R., "Experimental and Computational Investigation of a Linearly Pitching NACA 0012 in Reverse Flow," 72nd Forum of the AHS, May 2016.

[7]Hodara, J., Lind, A. H., Jones, A. R., and Smith, M. J., "Collaborative Investigation of the Aerodynamic Behavior of Airfoils in Reverse Flow," *J. American Helicopter Society*, Vol. 61, (3), Sep. 2015, pp. 1–15.

[8]Hiremath, N., Shukla, D., Raghav, V., and Komerath, N., "A Summary of the Flowfield Around a Rotor Blade in Reverse Flow," 72nd Forum of the AHS, May 2016.

[9]Berry, B. and Chopra, I., "Slowed Rotor Wind Tunnel Testing of an Instrumented Rotor at High Advance Ratio," 40th European Rotorcraft Forum, Sep. 2014.

[10]Datta, A., Yeo, H., and Norman, T. R., "Experimental Investigation and Fundamental Understanding of a Full-Scale Slowed Rotor at High Advance Ratios," *J. American Helicopter Society*, Vol. 58, (2), Apr. 2013.

[11]Potsdam, M., Datta, A., and Jayaraman, B., "Computational Investigation and Fundamental Understanding of a Slowed UH-60A Rotor at High Advance Ratios," 68th Annual Forum of the AHS, 1–3 May 2012.